

Enhanced and stable photoelectrochemical H₂ production using a engineered nano multijunction with Cu₂O photocathode



Shankara S. Kalanur ^{a,*}, Young Jae Lee ^b, Hyungtak Seo ^{a,b,**}

^a Department of Materials Science and Engineering, Ajou University, Suwon 443-739, Republic of Korea

^b Department of Energy Systems Research, Ajou University, Suwon 16499, Republic of Korea

ARTICLE INFO

Article history:

Received 30 March 2022

Received in revised form

24 May 2022

Accepted 5 June 2022

Available online 1 July 2022

Keywords:

Photocathode

NiO_x

MoO_x

Hole extraction

Photoelectrochemical water splitting

ABSTRACT

Cuprous oxide (Cu₂O) is one of the ideal photocathodes explored for solar water splitting applications due to its suitable optical properties and band edge positions. However, state-of-the-art Cu₂O employs Au back contact for hole extraction and Pt or Ru catalyst for water reduction reactions. Moreover, photo-corrosion of Cu₂O during the AM 1.5 G illumination is one of the serious challenges that limit the efficiency of water splitting reactions. In this work, a multijunction strategy in which the Cu₂O is sandwiched between the stoichiometrically engineered hole extraction layer and an efficient, non-toxic MoO_x catalyst layer is proposed for the enhanced charge separation and stable H₂ production activity. The optimized multijunction system exhibits the highest photocurrent of 6.1 mA cm⁻² at 0 V vs RHE reported for noble metal-free Cu₂O photocathodes. Furthermore, a significant anodic shift in onset potential was noticed. In the multijunction, the tuned layers of NiO_x, aluminum-doped zinc oxide, and MoO_x act as hole scavenger, electron tunneler, and H₂ catalyst, respectively. Importantly, the proposed nanolayers multijunction system demonstrates the effective utilization of noble metal and sulfide-free components for stable and enhanced H₂ productions employing Cu₂O photocathodes.

© 2022 Elsevier Ltd. All rights reserved.

1. Introduction

The current advances in the energy sector have indicated the dominance of energy storage devices in a wide range of applications, importantly in logistics and transportation [1]. Mainly, the advances in energy storage devices through electrical vehicles are expected to dominate in the coming decade due to their well-established technology and applications [2]. However, energy storage devices are generally derived from materials that are less abundant on the earth's surface (for example Li) and the stored energy drains with time [3]. Hence, a radical shift toward green, sustainable, renewable, and stable (non-depleting under stored conditions) energy technologies is essential that derived using earth-abundant, safe, and non-toxic materials [4]. Fortunately, hydrogen has demonstrated promising implementation as an energy source via fuel cell systems to produce electricity for industrial, households, and vehicles and thus implicating the future of energy [5,6]. Importantly, hydrogen is abundant and could be stored stably for a long time without decay and may well

potentially meet future energy demands. Hence, the hydrogen production technologies using renewable and sustainable pathways are expected to hold the key to establishing hydrogen infrastructure for feasible usability [7–11]. Among the various methods, photoelectrochemical (PEC) water splitting presents a clean, renewable, and sustainable route of producing hydrogen by utilizing abundant sources such as solar energy and water [12–14]. Therefore, significant advances in solar water splitting technology are essential to provide facile hydrogen production strategies for the future.

Efficient solar water splitting can be achieved using a variety of semiconductors that satisfy certain characteristic requirements concerning band gap, band edge positions, bulk charge, and transport properties [15,16]. Among the widely explored semiconductors, only a few materials satisfy all the essential conditions required to carry out overall water splitting activity [17]. Cuprous oxide (Cu₂O) is one such semiconductor characterized by p-type behavior possessing ideal bandgap and band edge positions to perform H₂ production by solar water splitting reactions. That is, Cu₂O possesses a direct bandgap of ~2 eV that could absorb the visible light until ~620 nm to produce the highest photocurrent of ~14.7 mA cm⁻², theoretically. Such absorption energy can drive ~18% efficiency of light-to-hydrogen conversion under simulated one sun conditions [18]. However, experimentally, achieving such a

* Corresponding author.

** Corresponding author.

E-mail addresses: shankarask@ajou.ac.kr (S.S. Kalanur), hseo@ajou.ac.kr (H. Seo).

high photocurrent is challenging due to the inefficient utilization of photogenerated charges at Cu₂O photocathodes. Moreover, Cu₂O undergoes rapid photo-corrosion under the illumination implying **significantly low stability during the water splitting conditions** [19]. Hence, Cu₂O photocathodes are generally implemented in the junctions supported by noble metal layers for effective charge collection, separation, and catalytic H₂ productions to increase photocurrent and stability under irradiation conditions [19].

The oxidation of Cu₂O to CuO occurs at a relatively lower potential (0.220 V) and proceeds rapidly using the photogenerated holes during the illumination [18]. Hence, the rapid extraction of holes from the Cu₂O valence band is essential for effective charge separation, which can be achieved using a hole extraction layer or back contact layers [18]. That is, Cu₂O photocathodes suffer from poor hole mobility and thus are generally deposited on a back contact containing an Au layer [18,20–22] or a hole extraction layer such as NiO, CuSCN [20,23] for effective charge collection and hole scavenging, respectively. Note that, the work function (in the case of Au) or the valence band (NiO and CuSCN) of the back contact should match with the valence band of Cu₂O for effective hole extraction on the conducting substrate. However, Au metal is expensive, less abundant, and shows absorption as well as strong reflection under the visible and infrared region of light that could affect the Cu₂O performance [20]. On the other hand, the reported NiO-based hole scavenger layer involves multiple steps and annealing processes [20], whereas the CuSCN is known to be environmentally toxic. Hence, an earth-abundant, less toxic having facile deposition protocol is essential to serve as an effective back contact and hole transport system for the Cu₂O photocathodes.

Furthermore, water reduction catalysts derived from noble metals such as Pt, Ru, and so on [18,20,22] are essential as electron extraction layers on Cu₂O photocathodes to carry out H₂ evolution reactions. Mainly, Cu₂O photoanodes show poor stability due to the surface instability with O²⁻ termination moieties and thus are coated with thin layers of oxides to avoid the direct contact of the Cu₂O surface with the aqueous electrolyte [19]. Like Au metal, Pt and Ru metals are not cost-effective and less abundant whereas the coating consisting of MoS₂ requires the use of toxic S element. Specifically, the synthesis of MoS₂ is generally achieved using S gases or S powders that could lead to the evolution of S-containing gases, whereas the use of S precursors in solution could lead to the unreacted residual S compounds. These gases and solutions containing S compounds are considered to be one of the toxic materials leading to air and soil/water pollution [24]. Mainly, the evolution of SO₂ gas is observed during the combustion of S-containing compounds or S powder, which is generally employed in the chemical vapor deposition synthesis of MoS₂ [25,26]. Hence, the release of SO₂ gas into the environment during such processing could interact with H₂O causing acid rain [24] and other health implications such as respiratory problems and climate change [24–27].

Therefore, a cheaper and nontoxic substitute is needed as an effective catalyst on the Cu₂O photocathodes for efficient electron extraction to drive the H₂ production reaction. Overall, an alternative material to the noble metals and toxic materials is required for the efficient and stable H₂ production activity for the Cu₂O photocathodes. Recently, the compositionally tuned NiO_x layer derived from sputtering has been found to offer efficient tunability of hole extraction properties due to the multivalence regulation of Ni [28]. On the other hand, the stoichiometrically tuned MoO_x has shown excellent catalytic activity toward the water reduction to the H₂ production reaction along with increased stability [29].

Given this, here we propose the utilization of both stoichiometrically engineered NiO_x and MoO_x as hole and electron extraction nanolayers, respectively, between the Cu₂O

photocathode for the enhanced and stable H₂ production activity. Initially, the NiO_x nanolayer was deposited using RF sputtering with optimized conditions followed by the electrodeposition of the Cu₂O layer under basic pH conditions. Finally, the Cu₂O was coated with aluminum-doped zinc oxide (AZO) and MoO_x layers successively using RF sputtering. The optimized NiO_x/Cu₂O/AZO/MoO_x multi-junction electrode exhibited the highest photocurrent of 6.1 mA cm⁻² at 0 V vs RHE. Furthermore, a significant enhancement in applied bias to photoconversion efficiency (ABPE) and incident photon to current efficiency was recorded. Importantly, the NiO_x/Cu₂O/AZO/MoO_x electrode showed an impressive anodic shift in onset potential with stable H₂ production under the AM 1.5 G illumination. A detailed band edge properties were evaluated using spectroscopic and electrochemical results to conclude the formation junction that facilitates active separation of photogenerated charges to carry out efficient water splitting to H₂ production reaction.

2. Experimental

2.1. Deposition of NiO_x

Before the deposition of the NiO_x nanolayer, the fluorine-doped tin oxide (FTO) substrates were cleaned and sonicated subsequently with water and ethanol. The RF magnetron sputtering of NiO_x was carried out at room temperature (~298 K) using high purity (99.99%) metallic Ni target in the presence of O₂ and Ar atmosphere. The various NiO_x deposition parameters were optimized by altering, the gas atmosphere, pressure, power watt, and time of deposition. The optimized deposition conditions involve a gas mixture flow ratio of Ar and O₂ of 20:12 sccm at a power of 100 W under the constant pressure of 1.2×10^{-2} bar with a deposition time of 20 min. Before the deposition, the unwanted deposition areas on the FTO surface are covered using 3 M tape. Before the deposition on the FTO substrate, a predeposition sputtering was carried out for 15 min with the substrate shutter closed to remove contaminants from the target surface and to attain stabilized growth rate. The substrate platform was kept on a rotating mode (30 rpm) for constant and uniform deposition of NiO_x. The power of sputtering was monitored throughout to check the reflected powers.

2.2. Deposition of Cu₂O

The Cu₂O electrodeposition on the FTO/NiO_x was carried out using the previously reported electrodeposition method [18]. The electrodeposition was carried out using FTO/NiO_x as working electrode, Ag/AgCl reference electrode, and Pt mesh counter electrode. An aqueous solution containing 0.2 M CuSO₄ (≥99%, Sigma Aldrich), 3 M lactic acid (≥85% Sigma Aldrich), and 0.5 M K₂HPO₄ (≥98% Sigma Aldrich) was used for the electrodeposition. The pH of the solution was adjusted to 12 by adding 2 M KOH (≥90%, Sigma Aldrich) solution. The deposition was carried out at an applied bias potential of -0.4 V (vs. Ag/AgCl) for 30 min at 60 °C (using a water bath). The abovementioned conditions for Cu₂O deposition were optimized based on the PEC characteristics. For each deposition, about 100 ml of deposition solution was used to deposit Cu₂O at 1 cm² of the area, and the deposition solution was used only once, and freshly prepared solutions were employed for each deposition.

2.3. Deposition of AZO

The deposition of AZO on FTO/NiO_x/Cu₂O was carried out using (optimized conditions) RF magnetron sputtering using an AZO target at room temperature (~298 K) in the presence of pure Ar

atmosphere (no O₂ was used) kept at a flow rate of 20 sccm. During the deposition, the power at the target was maintained at 100 W. The pressure in the deposition chamber was maintained constant at 2×10^{-2} bar, and the substrate was kept on a rotating mode (30 rpm) for uniform deposition. The exposed FTO part (undeposited) of the substrate was covered to avoid deposition of AZO directly on FTO. A predeposition sputtering condition opted as before was maintained (15 min with the substrate shutter closed) to remove contaminants from the target surface and to attain stabilized growth rate.

2.4. Deposition of MoO_x

The deposition condition for the MoO_x layer on FTO/NiO_x/Cu₂O/AZO was optimized based on the high and stable photocurrents produced. Pure MoO₃ target (99% purity) was used under an Ar atmosphere maintained at a flow of 20 sccm (no O₂ was used). The opted conditions are chamber pressure of 2×10^{-2} bar, room temperature (~298 K), and an input power of 100 W. The substrate was kept on a rotating mode (30 rpm) for constant deposition and the deposition was carried out at 15 min. The exposed FTO part of the substrate was covered to avoid deposition of MoO_x directly on the FTO substrate. A predeposition sputtering condition opted as before was maintained (15 min with the substrate shutter closed) to remove contaminants from the target surface and to attain stabilized growth rate.

2.5. Voltammetric measurements

The details of instruments used for the characterization are given in the supporting information file. The electrochemical measurements were carried out using a three-electrode system having FTO/NiO_x/Cu₂O/AZO/MoO_x as working electrode, Ag/AgCl reference electrode, and Pt counter electrode at room temperature (298 K). The electrode setup was installed in an airtight cell having quartz window. The buffered solution (pH $\sim 4.9 \pm 0.1$) of 1 M Na₂SO₄ having 0.1 M potassium phosphate was used for electrochemical measurements. The dissolved O₂ in the electrolyte was removed by N₂ bubbling for 30 min before the PEC measurements. Impedance measurements were carried at a bias voltage of 0 V (vs. RHE) between 0.001 and 1000 Hz with an amplitude of 5 mV. For the Mott-Schottky measurements, a frequency of 1000 Hz was used. The measured potentials vs Ag/AgCl were converted to standard RHE using the below equation:

$$E_{RHE} = E_{Ag/AgCl} + (0.0591 \times pH) + E_{Ag/AgCl}^0 \quad (1)$$

3. Results and discussion

3.1. Structural characterization

The RF magnetron sputtering offers an effective tuning of stoichiometry, valency, oxygen vacancies, and thickness with a facile control over the deposition area of a variety of materials. Specifically, the RF magnetron sputtering is found to be effective, as Cu₂O show limited stability based on electrolyte, pH, and temperature. Here, the deposition of NiO_x, AZO, and MoO_x is carried out at room temperature (298 K). To check the morphology of sputtered NiO_x, AZO, and MoO_x, the deposition was initially carried out directly on the FTO surface. Fig. 1a–f shows the surface morphology and thickness of the deposited materials optimized based on the PEC performance. Fig. 1a and d represents the surface and cross section of NiO_x on the FTO surface. The NiO_x opts for thin-film morphology having ~20 nm of thickness. On the other hand, the AZO and MoO_x

show a thickness of ~80 nm (Fig. 1e) and ~100 nm (Fig. 1f) having nanostructure morphology (Fig. 1b and c), respectively. Fig. S1 shows the low-resolution surface SEM images compared with the bare FTO for the confirmation of the deposition with a change in surface morphology. Furthermore, the low-resolution images reveal the uniform deposition throughout the FTO surface indicating the superior applicability of the sputtering technique in providing uniformly deposited materials over the larger surface area. The XRD pattern of NiO_x, AZO, and MoO_x on the FTO substrate shows no significant appearance due to the thin layer of the materials as depicted in Fig. 1g plotted with respect to the arbitrary scale. The black dots presented in the XRD pattern confirms the SnO₂ peaks of the substrate. The XRD pattern of the electrode-deposited Cu₂O confirms the cubic crystal phase-oriented along the (111) plane. The XRD pattern of the multijunction is presented in Fig. 1h. However, due to the thinner layer of NiO_x, AZO, and MoO_x in the Cu₂O junction, only the XRD peaks related to cubic Cu₂O and substrate appeared. The comparison of standard peaks with the measured XRD peaks is presented in Figs. S2 and S3.

To confirm the presence of AZO and MoO_x on the surface of Cu₂O, the change in surface structure and cross-section morphology was analyzed as shown in Fig. 2a–c. Fig. 2a shows the surface and cross-sectional SEM image of Cu₂O deposited on the NiO_x layer on the FTO substrate. The surface of Cu₂O appears to contain sharp-edged triangular surfaces arranged randomly having a smooth surface. The thickness of the Cu₂O was measured to be ~1.8–2 μm. However, the subsequent deposition of AZO and MoO_x on the Cu₂O surface causes a slight change in smoothness without causing a significant change in nanostructure morphology (Fig. 2b and c). The low-resolution SEM images of Cu₂O before the AZO and MoO_x are depicted in Fig. S4, confirming the uniform deposition of both AZO and MoO_x in thin layer format throughout the surface without affecting the surface nanostructure of Cu₂O. The magnified inset in the cross-sectional image of both NiO_x/Cu₂O/AZO and NiO_x/Cu₂O/AZO/MoO_x confirms the presence of AZO and MoO_x with a slight change in the surface smoothness. Furthermore, the cross-sectional SEM image was employed to map the individual elements as shown in Fig. 2d and e. As expected, the presence of Cu (Fig. 2f) was confirmed slightly above the FTO substrate whereas the Ni (Fig. 2g) was found only below the Cu and above the FTO substrate. Mainly, the presence of Zn (Fig. 2h) and Al (Fig. 2i) was confirmed above the Cu₂O surface, while the presence of O (Fig. 2j) was implicated in all the regions (including FTO). On the other hand, the presence of Mo (Fig. 2k) was confirmed at the surface of the Cu₂O. Furthermore, to support the quantitative existence of individual elements along with the thickness of the photocathode, the EDS analysis was performed as presented in Fig. 3. Fig. 3a shows the cross-sectional SEM image and the region of the area selected for quantitative analysis. The mapping and the % quantitative were analyzed along the line presented in Fig. 3b. The presence of Cu, O, Ni, Zn, Al, and Mo was confirmed along with the thickness as expected based on the deposition pattern (Fig. 3c). That is, the presence of Ni was found between the Cu₂O and the FTO substrate, whereas the presence of Zn, Al, and Mo is confirmed only at the surface. On the other hand, the O has appeared in all the regions. The EDX spectrum confirms the presence of materials without any impurity peaks. Mainly, the quantitative at% of individual elements are presented in the table in Fig. 3d.

3.2. Spectroscopic characterization

XPS analysis was performed to investigate the valency and composition of the deposited thin films. The measured XPS plots are calibrated using the C 1s reference peak at 285.65 eV. The high-resolution XPS of Cu 2p exhibits a doublet with a characteristic

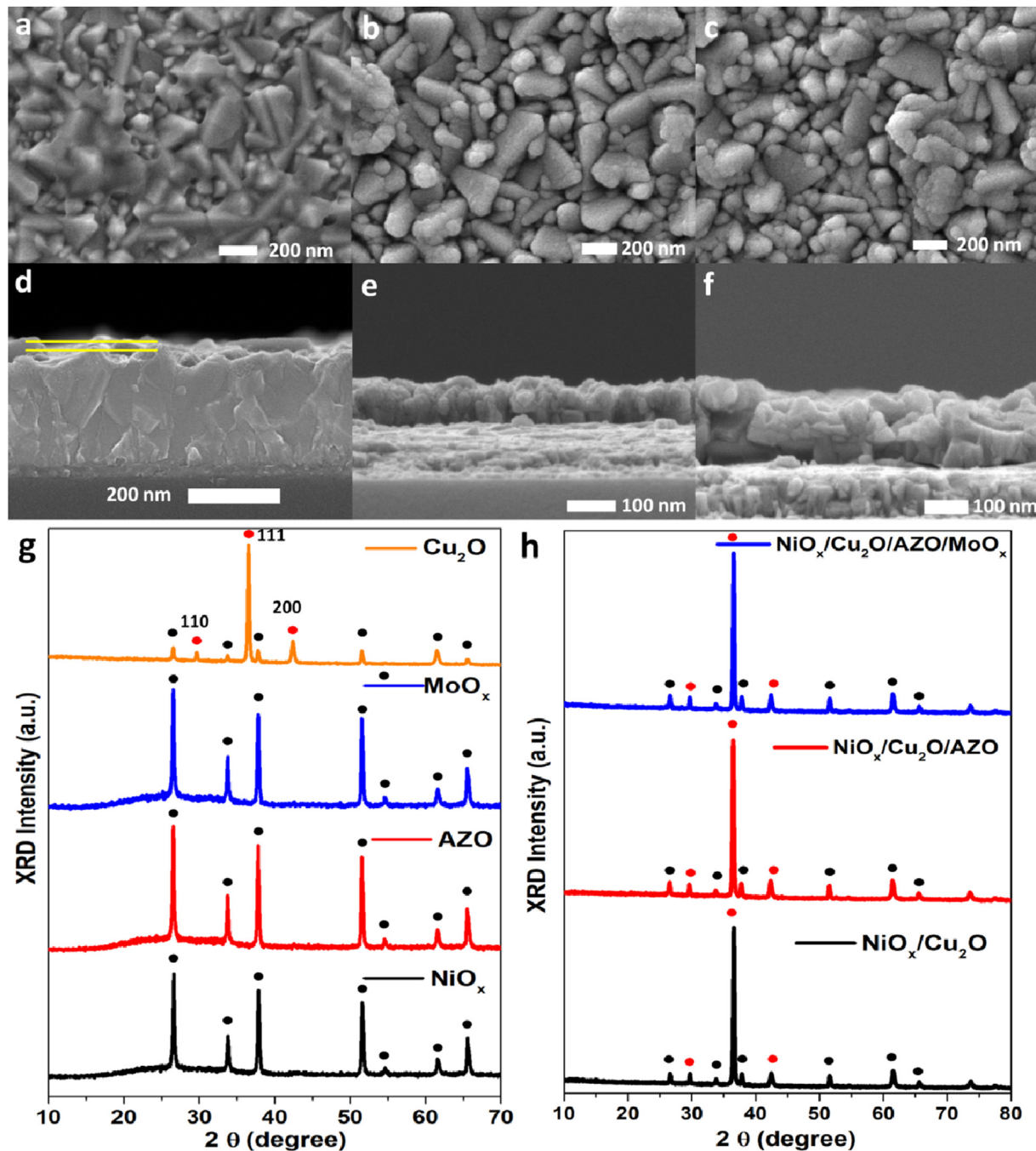


Fig. 1. High-resolution surface and cross-sectional FESEM surface image of (a and d) FTO/NiO_x, (b and e) FTO/AZO, and (c and f) FTO/MoO_x. (g) XRD of NiO_x, AZO, MoO_x, and Cu₂O single layer on FTO substrate. (h) XRD pattern of NiO_x/Cu₂O, NiO_x/Cu₂O/AZO, and NiO_x/Cu₂O/AZO/MoO_x heterojunctions on the FTO substrate. The peaks related to FTO substrate, Cu₂O, and NiO_x are indicated using black, red, and blue dots, respectively.

satellite peak as shown in Fig. 4a. The doublet peaks situated at a binding energy of 932.27 and 952.11 eV are ascribed to the splitting energy of Cu 2p_{3/2} and Cu 2p_{1/2}, respectively. The peaks were further deconvoluted to confirm the presence of valency. Upon deconvolution, the doublet appeared with major and minor peaks as shown in Fig. 4a. The high-intensity peaks confirm the formation of Cu(I) species present in cubic Cu₂O crystal, whereas the adjacent low-intensity peaks could be indexed to either minor presence of Cu(II) state of CuO moiety or the surface Cu(OH)₂ species adsorbed due to basic pH deposition condition [30,31]. The peaks that appeared between the energy values of 940 and 948 eV are indexed

to the characteristic satellite peaks of Cu 2p. The high-resolution O 1s spectra of Cu₂O film are presented in Fig. 4b. The deconvolution of O 1s peak yields a high-intensity peak at 530.73 eV due to lattice Cu–O of Cu₂O crystal, whereas the low-intensity peak appeared at 532.13 was assigned the external –OH group or adsorbed water species at the surface [30]. The sputtered hole scavenging underlayer was characterized to evaluate the valency of Ni states. Fig. 4c presents the high-resolution XPS graph of the NiO_x layer indicating the splitting of 2p_{3/2} and 2p_{1/2} along with the respective satellite peak. The deconvoluted peaks that appeared at 854.12 and 871.78 represent the 2p_{3/2} and 2p_{1/2} splitting of Ni (II) state, whereas the

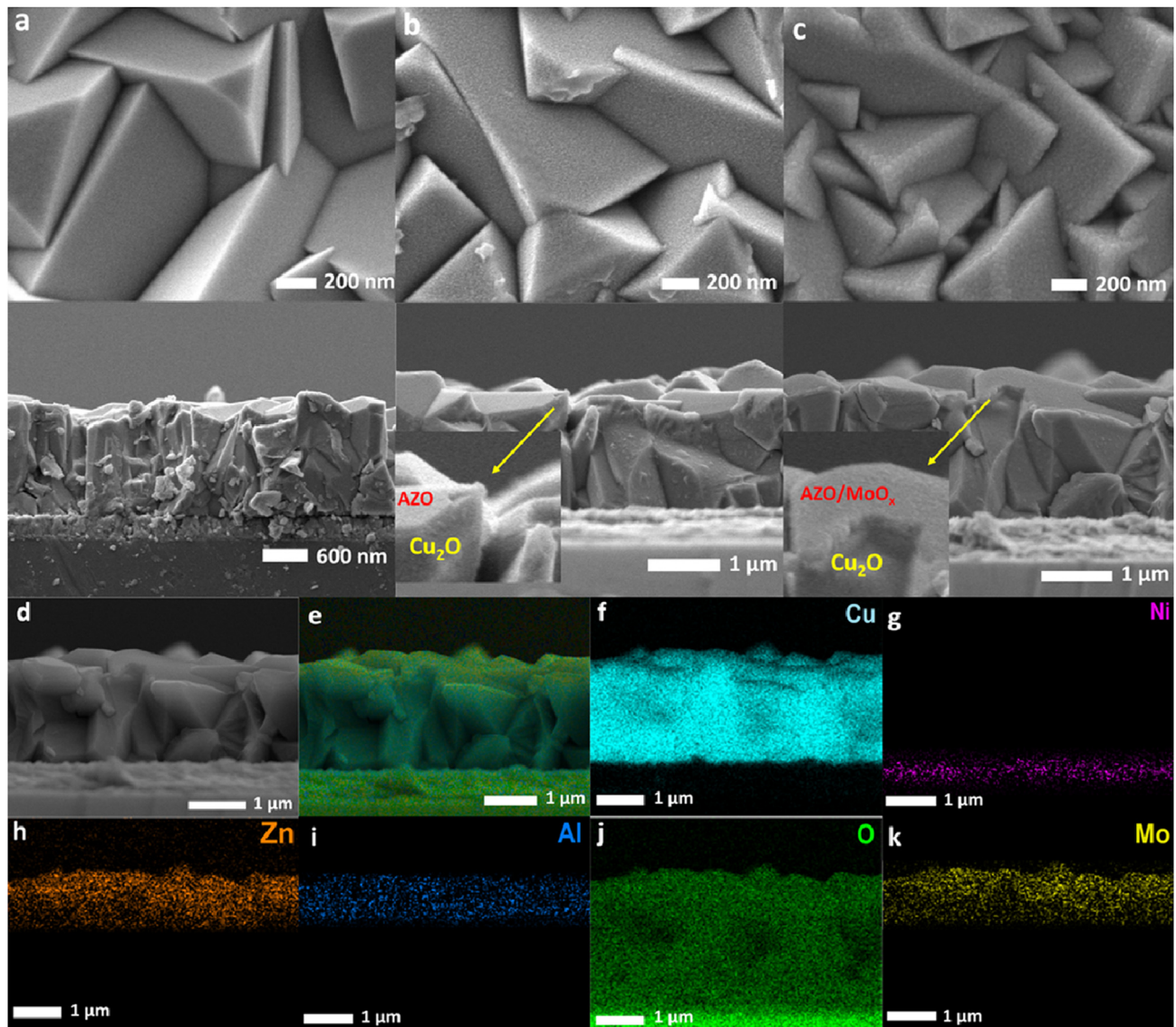


Fig. 2. High-resolution surface and cross-sectional FESEM surface image of (a) $\text{NiO}_x/\text{Cu}_2\text{O}$, (b) $\text{NiO}_x/\text{Cu}_2\text{O}/\text{AZO}$, and (c) $\text{NiO}_x/\text{Cu}_2\text{O}/\text{AZO}/\text{MoO}_x$ on FTO substrate. The inset in (b) and (c) shows a magnified view showing the deposited AZO and MoO_x . (d) Cross-sectional topography of $\text{NiO}_x/\text{Cu}_2\text{O}/\text{AZO}/\text{MoO}_x$ with (e) overall mapping and distribution presentation of (e) Cu, (f) Ni, (g) Zn, (h) Al, (i) O, and (j) Mo elements.

peaks at 855.98 and 873.92 eV confirm the presence of Ni (III) state of $2\text{p}_{3/2}$ and $2\text{p}_{1/2}$ splitting, respectively [28]. Furthermore, the peaks observed at 861.18 and 879.39 eV indicate the satellite peaks corresponding to the $2\text{p}_{3/2}$ and $2\text{p}_{1/2}$ splitting. The deconvolution of O 1s XPS peak splitting in the NiO_x films shows the presence of three major peaks at 529.22, 531.02, and 532.29 eV due to the oxygen presence in Ni–O, Ni–OH (oxygen vacancy), and surface adsorbed O, respectively.

The XPS peaks of the AZO layer deposited on the Cu_2O were deconvoluted as shown in Fig. 4e. The doublet having the peaks at the binding energy values of 1022.26 and 1045.42 eV indicate the splitting of Zn $2\text{p}_{3/2}$ and Zn $2\text{p}_{1/2}$, respectively [32]. The absence of subpeaks in the deconvoluted graph indicates the presence of only the Zn (II) state in the layer. The XPS peak of the Al-doped in the AZO layer was presented in Fig. 4f. The weak intensity singlet appeared at 73.96 eV, indicating the presence of an Al (III) state due to the presence of relatively low concentration [33,34]. Similarly, the O 1s peak deconvoluted at the AZO layer is shown in Fig. 4g. Interestingly, the adsorbed O peak was

found to show high intensity compared to the lattice O implicating the dominant –OH group due to the deposition of AZO under the inert atmosphere. Fig. 4h represents the high-resolution XPS peak of the Mo 3d spectrum showing a doublet with the splitting of Mo $3\text{d}_{5/2}$ and Mo $3\text{d}_{3/2}$ at 232.77 and 235.89 eV, respectively. The deconvolution produces a high-intensity doublet at high binding energy values and a low-intensity doublet at low binding energy values confirming the dominance of Mo (VI) and the minor presence of Mo (IV), thus implicating the presence of oxygen vacancies in the MoO_x layer [35–37]. The presence of oxygen vacancies was further confirmed via the deconvolution of the O 1s peak obtained from the XPS graph of MoO_x layers. Fig. 4i shows the deconvoluted O 1s spectra producing 3 distinguishable peaks. The high-intensity peak at a lower binding energy value indicates the presence of lattice O bonded to Mo, whereas the moderate-intensity peak indicates the presence of oxygen vacancies in the lattice. The low-intensity peak that appeared at higher binding energy values confirms the presence of adsorbed oxygen.

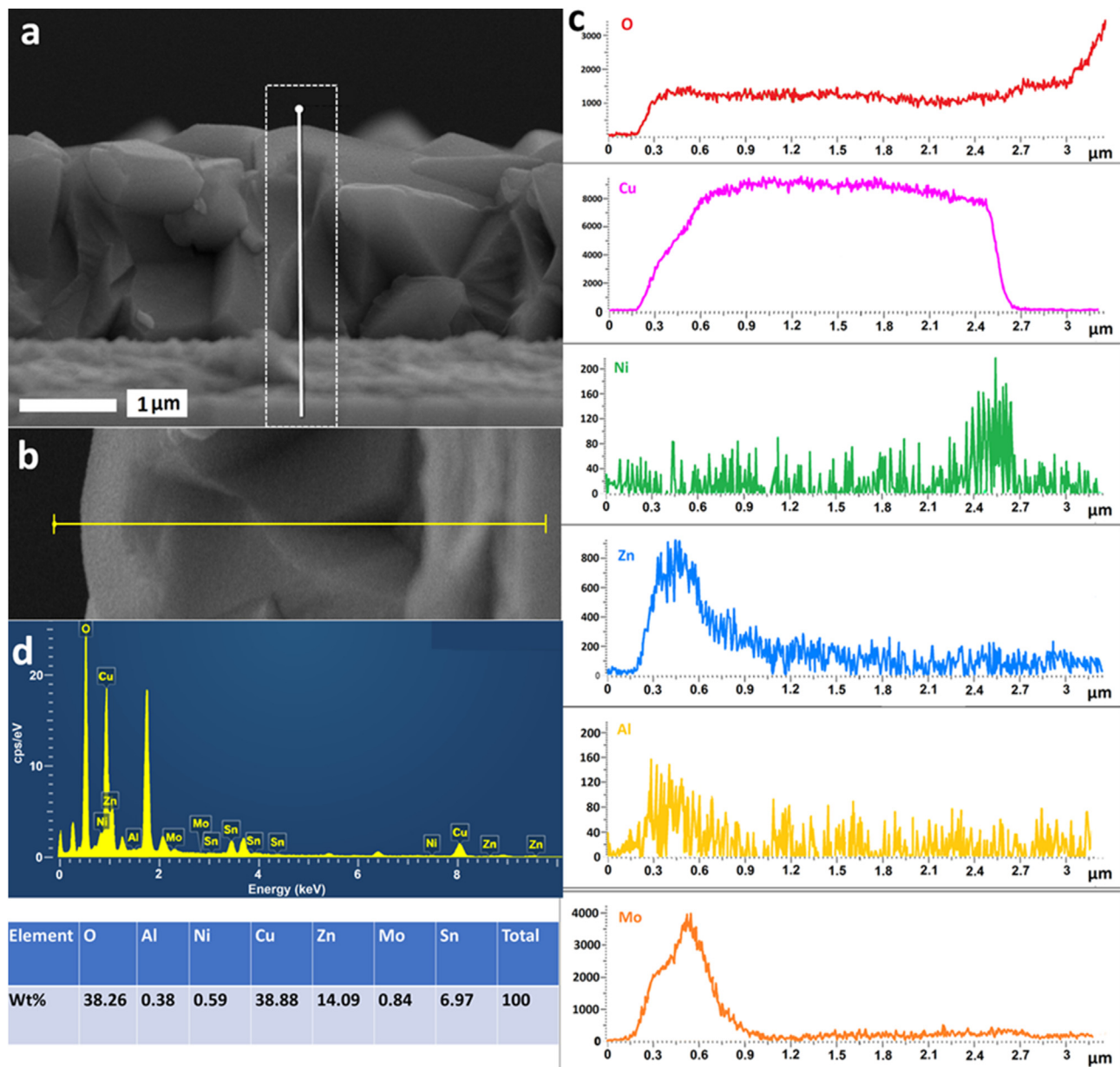


Fig. 3. Cross-sectional SEM image selected for elemental profiling. (b) The selected portion and the line represent the profile of elemental mapping. (c) Elemental profiling along the thickness represents the presence of O, Cu, Ni, Zn, Al, and Mo, along with the height of films. (d) EDX spectrum and wt% of the elements present in thin films.

The UV-visible absorption spectra of Cu_2O and NiO_x are presented in Fig. 5a. The NiO_x shows the absorption onset of ~350 nm with tailing due to the presence of oxygen vacancies and multiple valencies of the Ni state, whereas the Cu_2O shows the absorption onset at 640 nm. Similarly, both AZO and MoO_x show the adsorption onset at ~400 nm with tailing due to the presence of oxygen vacancies (Fig. 5b). However, in the multijunction system such as $\text{NiO}_x/\text{Cu}_2\text{O}$, $\text{NiO}_x/\text{Cu}_2\text{O}/\text{AZO}$, and $\text{NiO}_x/\text{Cu}_2\text{O}/\text{AZO}/\text{MoO}_x$ the onset of the absorption appears at 640 nm. Based on Tauc's plot the bandgap of NiO_x (Fig. 5d), Cu_2O (Fig. 5d), AZO (Fig. 5e), and MoO_x (Fig. 5e) are calculated to be 3.22, 2.30, 3.33, and 3.30 eV, respectively. In the multijunction system, the band gap was found to be ~2.3 eV (Fig. 5f). The XPS valence band edge plot was measured to assess the energy difference between the valence band and the Fermi level that determines the type of semiconductor junction on the electrode. The valence band edge of NiO_x and Cu_2O was calculated to be

at ~0.1 and 0.2 eV from the Fermi level as shown in Fig. 5g. That is, both NiO_x and Cu_2O confirm the p-type characteristics confirming the presence of Fermi level near the valence band edge. Similarly, the XPS valence band edge plot of AZO and MoO_x shows the presence of Fermi level near the conduction band thus confirming the n-type characteristics. The energy difference between the valence band and Fermi level was calculated to be ~3.1 and ~2.73 eV for the AZO and MoO_x electrodes (Fig. 5h). However, in the multijunction system, the surface of the electrode shows a slight difference in XPS valence band edge plots due to the alignment of the Fermi level between the materials after the heterojunction formation. As depicted in Fig. 5i, the Fermi level of Cu_2O deposited on the NiO_x shows a slight decrease to 0.13 eV. On the other hand, the XPS valence band edge value of AZO and MoO_x upon the subsequent deposition on $\text{NiO}_x/\text{Cu}_2\text{O}$ shows the value of 2.50 and 2.67 eV indicating the change in Fermi level due to heterojunction

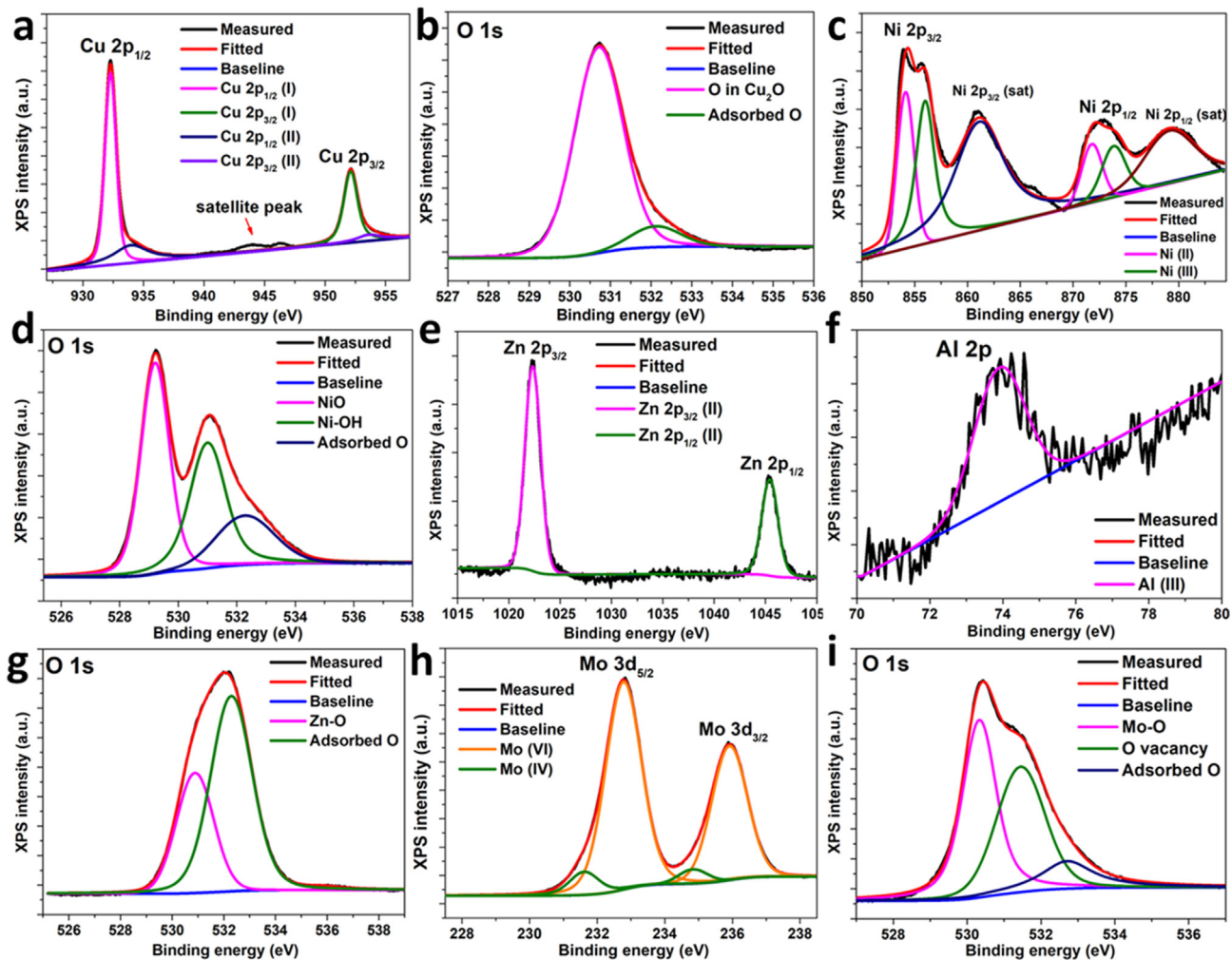


Fig. 4. Deconvoluted XPS spectra of (a) Cu 2p, (b) O 1s in Cu₂O, (c) Ni 2p, (d) O 1s in NiO_x, (e) Zn 2p, (f) Al 2p, (g) O 1s in AZO, (h) Mo 3d, and (i) O 1s in MoO_x.

formation (Fig. 5i). The formation of such a junction is known to provide effective separation of photogenerated electrons and holes for efficient water splitting activity [28].

3.3. Photoelectrochemical studies

The most significant advantages of the proposed nanolayer multijunction were revealed upon PEC characterization as shown in Fig. 6. The bare Cu₂O photocathode deposited directly on the FTO substrate shows the highest photocurrent of $\sim 3 \text{ mA cm}^{-2}$ (at 0 V vs RHE) with a photocurrent onset of 0.5 V. The presence of a stoichiometrically tuned NiO_x layer beneath the Cu₂O film causes a significant shift in the photocurrent onset toward the anodic direction (0.67 V) along with the increase in the photocurrent to 4.4 mA cm^{-2} (at 0 V vs RHE). However, the deposition of AZO causes a drastic decrease in photocurrent that could be ascertained to the inefficient utilization of electrons to drive H₂ production reactions at the AZO surface. Importantly, the deposition of MoO_x causes an impressive increase in photocurrent values to $\sim 6.1 \text{ mA cm}^{-2}$ (at 0 V vs RHE) with a remarkable anodic shift in onset potential (Fig. 6a). The obtained photocurrent value is found to be the highest value reported for Cu₂O photocathodes tested without the use of non-noble metal-derived catalyst and Au back contact. The obtained photocurrent is one of the highest and comparable to the results obtained using noble metal catalysts. Importantly, the optimized

NiO_x/Cu₂O/AZO/MoO_x electrode shows an onset potential of $\sim 0.76 \text{ V}$ indicating the catalytic effect of MoO_x toward solar water reduction to H₂ production reaction.

The ABPE was calculated for the Cu₂O photocathodes as shown in Fig. 6b. The Cu₂O photocathodes without the presence of MoO_x show lower photoconversion efficiencies, whereas the NiO_x/Cu₂O/AZO/MoO_x exhibited the highest ABPE of 1.75% at 0.5 V vs. RHE. Stability is one of the serious concerns of Cu₂O photocathodes. The stability was investigated at a bias voltage of 0 (vs. RHE) under AM 1.5 G illumination as shown in Fig. 6c the pristine Cu₂O and the NiO_x/Cu₂O photocathodes exhibited poor stability due to the rapid photo-corrosion under the illumination. That is, more than 50% of the initial photocurrent shows a decrease within 2 h of the illumination. Even though the NiO_x/Cu₂O/AZO exhibited significant stability (Fig. 6c and S5), no enhancement in the photocurrent was noticed due to the poor water reduction catalytic reaction at the AZO surface (blue line in Fig. 6c and S5). On the other hand, NiO_x/Cu₂O/AZO/MoO_x showed excellent stability under prolonged illumination conditions. To investigate the effect of AZO in the junction, the MoO_x was directly deposited on the Cu₂O photocathode, and the I-t measurements were carried out under the illumination. Interestingly, the layer of MoO_x on Cu₂O shows significant enhancement in the photocurrent, however, the stability remained poor exhibiting a rapid decrease in photocurrent due to photo-corrosion (Fig. S5). This indicates that the AZO layer acts as an

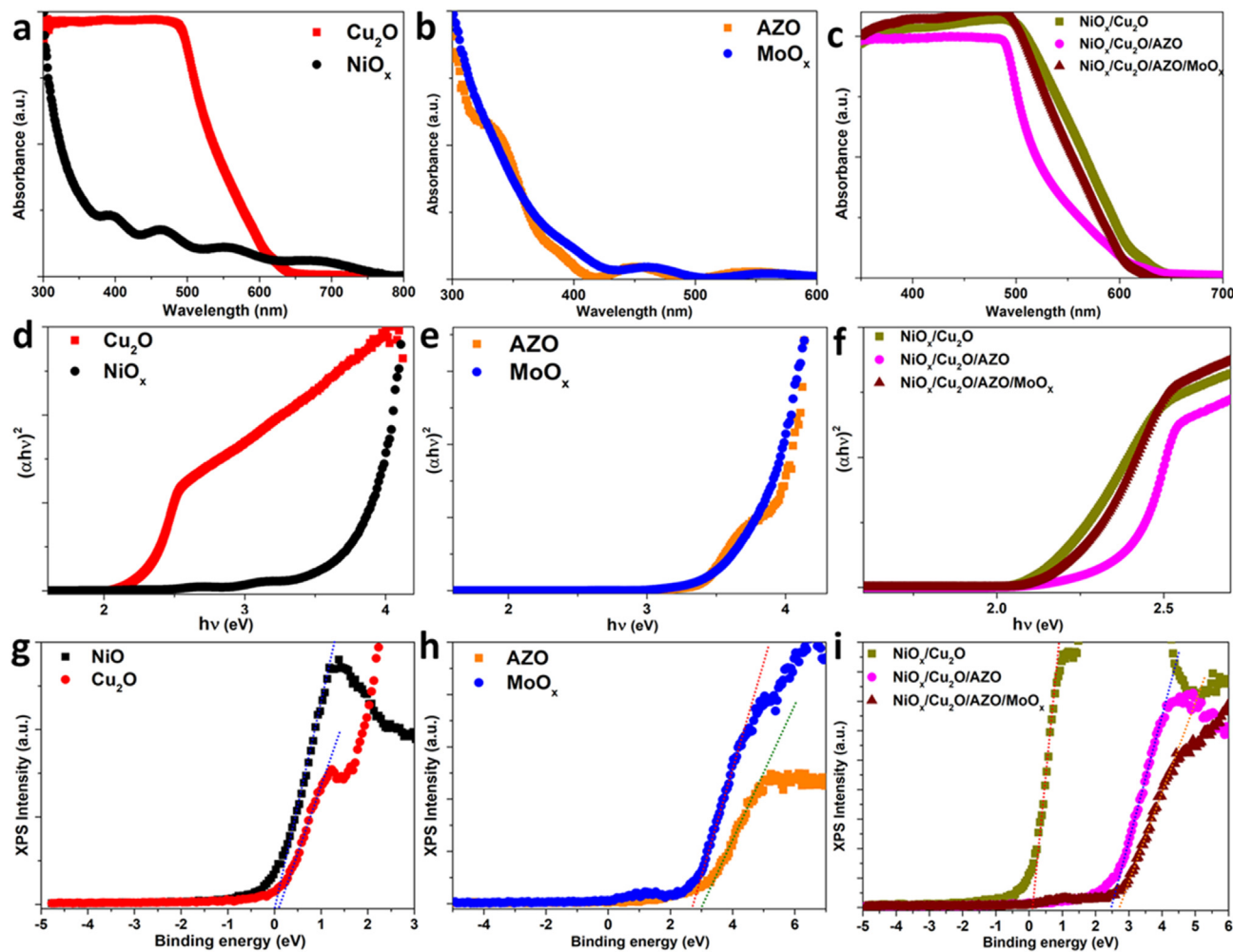


Fig. 5. Absorbance (a, b, and c), Tauc's plot (d, e, and f), and XPS valence band edge (g, h and i) plot of (NiO_x , Cu_2O), (AZO, MoO_x), and ($\text{NiO}_x/\text{Cu}_2\text{O}$, $\text{NiO}_x/\text{Cu}_2\text{O}/\text{AZO}$, $\text{NiO}_x/\text{Cu}_2\text{O}/\text{AZO}/\text{MoO}_x$) electrodes, respectively.

electron tunneling layer and increases the stability by encapsulating the Cu_2O surface to avoid direct contact with electrolytes.

Fig. 6d shows the incident photon-to-current conversion efficiency (IPCE) plot of $\text{NiO}_x/\text{Cu}_2\text{O}/\text{AZO}/\text{MoO}_x$ photoelectrode. The reliable IPCE measurements for other electrodes (Cu_2O , $\text{NiO}_x/\text{Cu}_2\text{O}$, $\text{NiO}_x/\text{Cu}_2\text{O}/\text{AZO}$, and $\text{NiO}_x/\text{Cu}_2\text{O}/\text{MoO}_x$) were not measured due to the rapid photo-corrosion caused during the illumination. Fig. 6d shows the wavelength response range of the optimized electrode measured at 0 V vs RHE. A maximum IPCE of about ~60% was produced up to 500 nm. The measured IPCE values were integrated using a standard AM 1.5 G spectrum to validate the LSV measurements. The IPCE integration produced a photocurrent of ~6 mA cm⁻² that validates the PEC measurements. Furthermore, impedance measurements were performed to evaluate the charge transfer resistance values at the electrolyte interface. Compared to the pristine Cu_2O , the $\text{NiO}_x/\text{Cu}_2\text{O}/\text{AZO}/\text{MoO}_x$ photoelectrode exhibited a smaller semicircle region implicating a decrease in charge transfer resistance at the junction/electrolyte interface (Fig. S6a). Note that, no evolution of H_2 was observed on the electrodes other than $\text{NiO}_x/\text{Cu}_2\text{O}/\text{AZO}/\text{MoO}_x$ due to poor stability and catalytic H_2 evolution reaction. The evolution of H_2 was observed due to the effective catalytic effect of MoO_x [29] with a faradaic efficiency of ~80% (Fig. S6b). Table S1 shows the comparison results of the $\text{NiO}_x/\text{Cu}_2\text{O}/\text{AZO}/\text{MoO}_x$ junction and the literature systems confirming the advantages of the proposed multijunction system.

3.4. Band edge properties

The band edge properties of the individual and the heterojunctions were evaluated using the Mott-Schottky (MS) analysis and measured XPS valence band edge and bandgap values given in the previous section. The intercept lines to the applied potential axis drawn to the MS curves typically demonstrate the presence of approximate location present at the difference value of ~0.1 V regarding conduction or valence band edge based on the n-type or p-type semiconductor thin films, respectively. Fig. 7a shows the MS plot of NiO_x thin film deposited on the FTO substrate. The negative slopes indicate the p-type characteristics of NiO_x that agree with the XPS valence band edge results that yield the intercept at ~1.02 V (vs RHE) indicating the proximity of the valence band edge. The MS plot of pristine Cu_2O (Fig. 7b) demonstrates the negative slope due to the presence of holes as charge carriers with an intercept value of ~0.42 V. On the other hand, both the AZO (Fig. S7) and MoO_x (Fig. 7c) exhibited a positive slope confirming the n-type characteristic and electron as charge carries with an intercept value of 0.38 and 0.20 V, respectively. Based on these values, the valence band of NiO_x , and Cu_2O , whereas the conduction band of AZO and MoO_x are plotted as shown in Fig. 8a. Note that, these band edge positions represent approximate positions before the formation of the heterojunction. However, upon the heterojunction formation the band alignment changes due to the Fermi

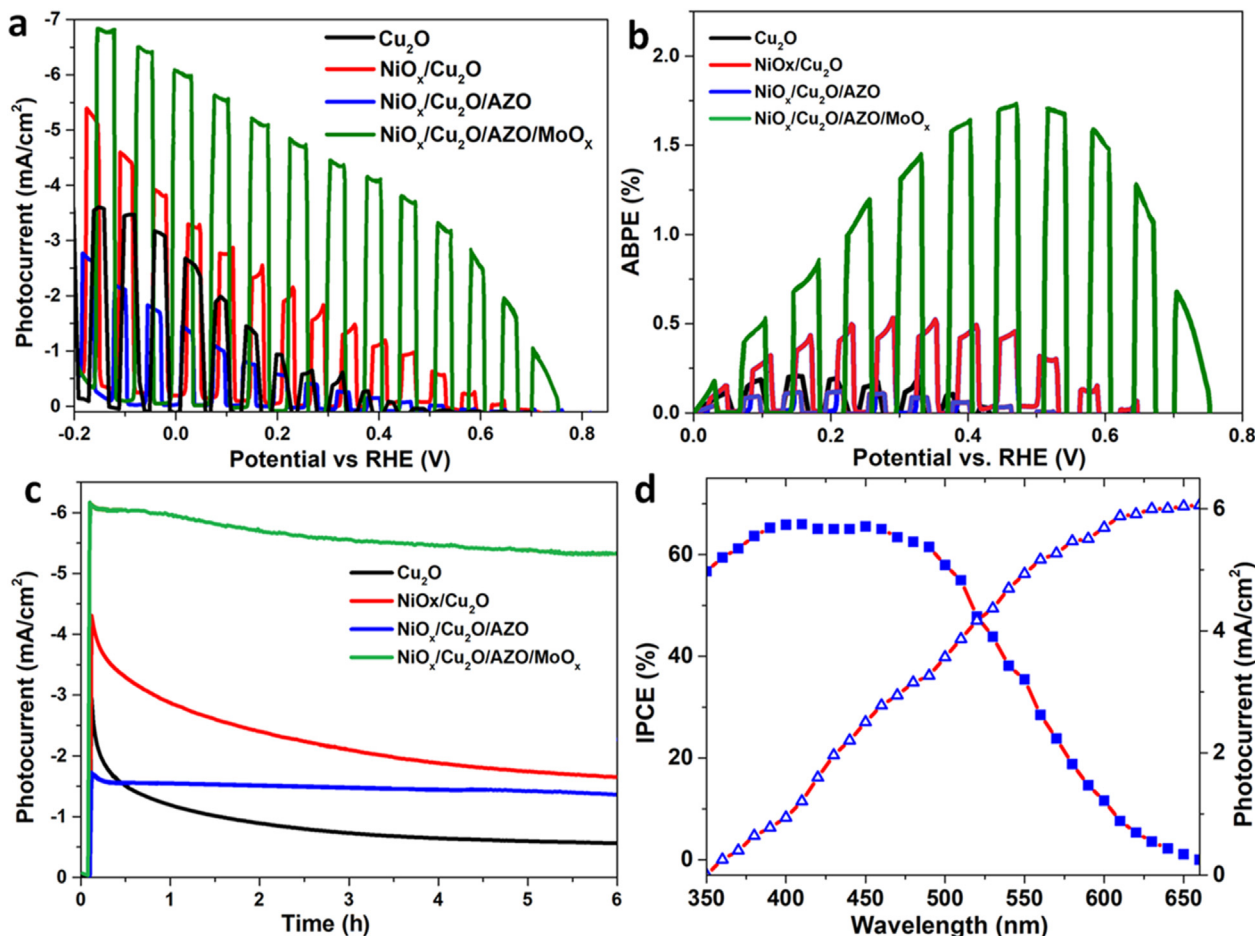


Fig. 6. (a) LSV, (b) ABPE, and (c) I-t stability of Cu_2O , $\text{NiO}_x/\text{Cu}_2\text{O}$, $\text{NiO}_x/\text{Cu}_2\text{O}/\text{AZO}$, and $\text{NiO}_x/\text{Cu}_2\text{O}/\text{AZO}/\text{MoO}_x$ photoelectrodes. (d) IPCE plot of $\text{NiO}_x/\text{Cu}_2\text{O}/\text{AZO}/\text{MoO}_x$.

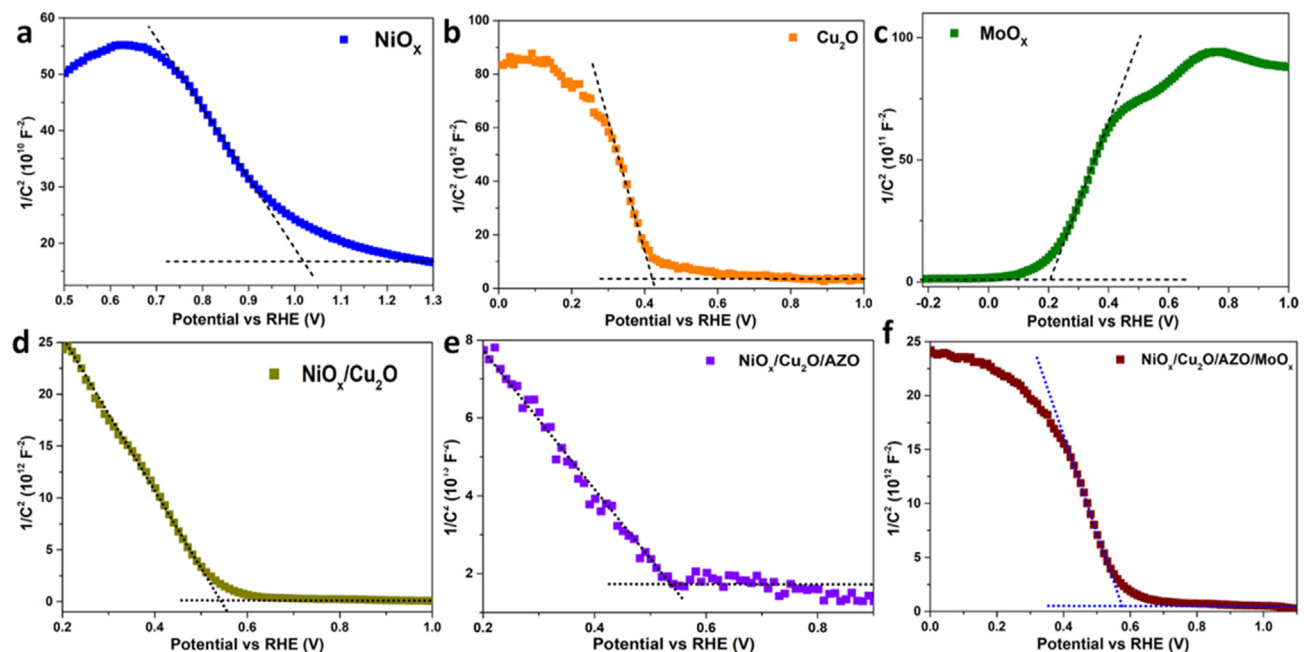


Fig. 7. MS plot of (a) FTO/ NiO_x , (b) FTO/ Cu_2O , (c) FTO/ MoO_x , (d) FTO/ $\text{NiO}_x/\text{Cu}_2\text{O}$, (e) FTO/ $\text{NiO}_x/\text{Cu}_2\text{O}/\text{AZO}$, and (f) FTO/ $\text{NiO}_x/\text{Cu}_2\text{O}/\text{AZO}/\text{MoO}_x$.

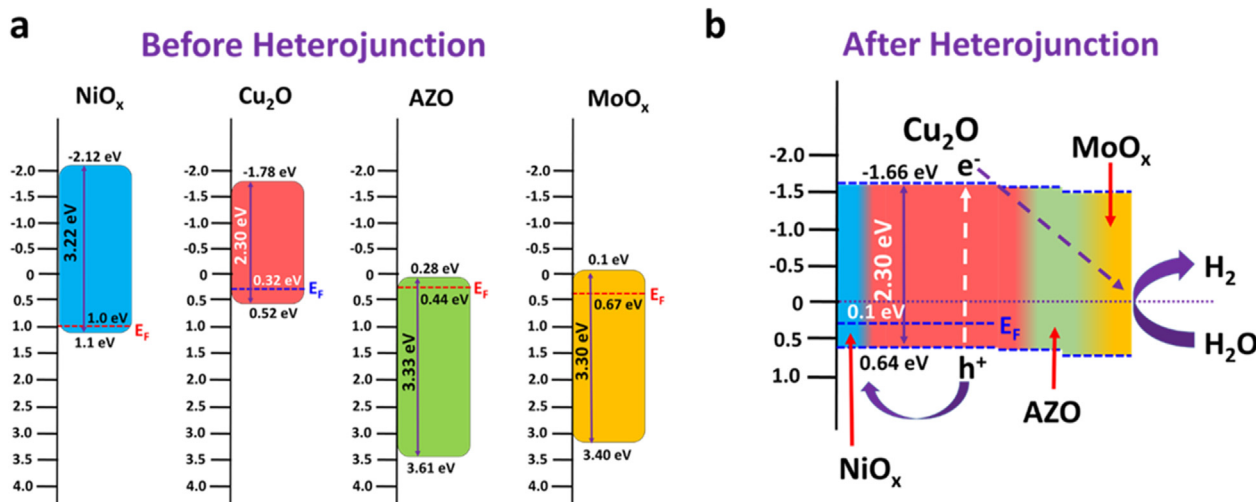


Fig. 8. Band edge plot of FTO/NiO_x, FTO/Cu₂O, FTO/AZO, FTO/MoO_x, FTO/NiO_x/Cu₂O, FTO/NiO_x/Cu₂O/AZO, and FTO/NiO_x/Cu₂O/AZO/MoO_x before (a) and after (b) the heterojunction formation indicating the dynamics of photogenerated carriers in the sandwiched multijunction electrode.

level adjustment. Due to the combination of two p-type materials in the junction, the overall MS curve shows a negative slope as shown in Fig. 7d indicating surface p-type characteristics with downward band bending. However, the intercept of the heterojunction shows an anodic shift upon heterojunction formation compared to the pristine Cu₂O. Interestingly, even upon the n-type AZO and MoO_x layer deposition on the p-type Cu₂O, the overall characteristics of the heterojunction remained as p-type as shown in Fig. 7e and d implicating downward band bending at the electrolyte interface. This could be due to the thinner layer of AZO and MoO_x on the Cu₂O surface acting as an electron tunneler and catalyst, respectively instead of the junction. That is, the MS intercepts of NiO_x/Cu₂O/AZO and NiO_x/Cu₂O/AZO/MoO_x are observed to be at 0.38 and 0.2 V, respectively indicating the presence of a downward shifted valence band of Cu₂O due to the presence of AZO and MoO_x on the surface. Therefore, based on the surface band edge changes of Cu₂O caused by the deposition of the AZO and MoO_x, the introduced gradient effect at the electrolyte interface is presented in Fig. 8b. Overall, the presence of a hole scavenger layer drags the photogenerated holes from the valence band of Cu₂O toward the substrate, whereas the photogenerated electrons are tunneled through the AZO toward the MoO_x catalyst to carry out the water reduction to H₂ production reactions. In this junction, the NiO_x, AZO, and MoO_x act as, hole scavenger, electron tunneler, and catalyst, respectively to enhance the PEC water splitting activity of Cu₂O.

4. Conclusion

To increase the PEC properties and stability of the Cu₂O photocathode, a multijunction strategy is proposed consisting of stoichiometrically tuned NiO_x, AZO, and MoO_x nanolayers. The initial fabrication process involves the RF magnetron sputtering of NiO_x on the substrate followed by the electrodeposition of Cu₂O under lactic stabilized basic conditions. Both the AZO and MoO_x were deposited on NiO_x/Cu₂O successively to form NiO_x/Cu₂O/AZO/MoO_x multijunction photocathode. Here, the NiO_x, AZO, and MoO_x nanolayers were optimized to yield higher PEC activity. Detailed characterization was performed to understand the structural, optical, and valence state properties of different single-layer and multijunction layers. The optimized NiO_x/Cu₂O/AZO/MoO_x multijunction photocathode exhibited the highest photocurrent of ~6.1 mA cm⁻² along with prolonged stability under the AM 1.5 G

illumination. The PEC study indicates that the NiO_x, AZO, and MoO_x act as, hole scavenger, electron tunneler, and catalyst, respectively to enhance the PEC water splitting activity of Cu₂O. Using spectroscopic and MS analysis, the probable band edge properties were evaluated to propose a gradient deviated Cu₂O layer at the surface that allows the effective charge separation of photogenerated charges via electron tunnelling and catalytic H₂ production effect. Importantly, the present approach proposes a facile fabrication process of Cu₂O photocathode multijunction involving the noble metal and sulfide free material contacts to carry out efficient and stable solar H₂ production.

Data availability statement

The raw/processed data required to reproduce these findings cannot be shared at this time as the data also forms part of an ongoing study.

Credit authors' statement

Shankara S. Kalanur: Writing, Validation, Investigation, Writing - original draft, Methodology. **Hyungtak Seo:** Revision, Supervision, Editing final draft. **Young Jae Lee:** Revision, Literature survey.

Declaration of competing interest

The authors declare that they have no known competing financial interests or personal relationships that could have appeared to influence the work reported in this paper.

Acknowledgments

This work was supported by the basic Research & Development program [2020R1F1A1054084] and C1 Gas Refinery Program (2015M3D3A1A01064899) through the National Research Foundation of Korea (NRF) funded by the Ministry of Science and ICT, the Republic of Korea.

Appendix A. Supplementary data

Supplementary data to this article can be found online at <https://doi.org/10.1016/j.mtchem.2022.101031>.

References

- [1] E. Karden, S. Ploumen, B. Fricke, T. Miller, K. Snyder, Energy storage devices for future hybrid electric vehicles, *J. Power Sources* 168 (2007) 2–11, <https://doi.org/10.1016/j.jpowsour.2006.10.090>.
- [2] O. Schmidt, A. Hawkes, A. Gambhir, I. Staffell, The future cost of electrical energy storage based on experience rates, *Nat. Energy* 2 (2017) 1–8, <https://doi.org/10.1038/nenergy.2017.110>.
- [3] V. Etacheri, R. Marom, R. Elazari, G. Salitra, D. Aurbach, Challenges in the development of advanced Li-ion batteries: a review, *Energy Environ. Sci.* 4 (2011) 3243–3262, <https://doi.org/10.1039/C1EE01598B>.
- [4] M.A. Pellow, C.J.M. Emmott, C.J. Barnhart, S.M. Benson, Hydrogen or batteries for grid storage? A net energy analysis, *Energy Environ. Sci.* 8 (2015) 1938–1952, <https://doi.org/10.1039/C4EE04041D>.
- [5] O.V. Marchenko, S.V. Solomin, The future energy: hydrogen versus electricity, *Int. J. Hydrog. Energy.* 40 (2015) 3801–3805, <https://doi.org/10.1016/j.ijhydene.2015.01.132>.
- [6] A. Chapman, K. Itaoka, K. Hirose, F.T. Davidson, K. Nagasawa, A.C. Lloyd, M.E. Webber, Z. Kurban, S. Managi, T. Tamaki, M.C. Lewis, R.E. Hebner, Y. Fujii, A review of four case studies assessing the potential for hydrogen penetration of the future energy system, *Int. J. Hydrog. Energy.* 44 (2019) 6371–6382, <https://doi.org/10.1016/j.ijhydene.2019.01.168>.
- [7] M. El-Shafie, S. Kambara, Y. Hayakawa, Hydrogen production technologies overview, *J. Power Energy Eng.* 7 (2019) 107, <https://doi.org/10.4236/jpee.2019.71007>.
- [8] J.D. Holladay, J. Hu, D.L. King, Y. Wang, An overview of hydrogen production technologies, *Catal. Today* 139 (2009) 244–260, <https://doi.org/10.1016/j.cattod.2008.08.039>.
- [9] Z. Wang, R.R. Roberts, G.F. Naterer, K.S. Gabriel, Comparison of thermochemical, electrolytic, photoelectrolytic and photochemical solar-to-hydrogen production technologies, *Int. J. Hydrog. Energy.* 37 (2012) 16287–16301, <https://doi.org/10.1016/j.ijhydene.2012.03.057>.
- [10] S.K. Thengane, A. Hoadley, S. Bhattacharya, S. Mitra, S. Bandyopadhyay, Cost-benefit analysis of different hydrogen production technologies using AHP and Fuzzy AHP, *Int. J. Hydrog. Energy.* 39 (2014) 15293–15306, <https://doi.org/10.1016/j.ijhydene.2014.07.107>.
- [11] I. Dincer, C. Acar, Review and evaluation of hydrogen production methods for better sustainability, *Int. J. Hydrog. Energy.* 40 (2015) 11094–11111, <https://doi.org/10.1016/j.ijhydene.2014.12.035>.
- [12] S. Chen, D. Huang, P. Xu, W. Xue, L. Lei, M. Cheng, R. Wang, X. Liu, R. Deng, Semiconductor-based photocatalysts for photocatalytic and photoelectrochemical water splitting: will we stop with photocorrosion? *J. Mater. Chem. A.* 8 (2020) 2286–2322, <https://doi.org/10.1039/C9TA12799B>.
- [13] M.G. Walter, E.L. Warren, J.R. McKone, S.W. Boettcher, Q. Mi, E.A. Santori, N.S. Lewis, Solar water splitting cells, *Chem. Rev.* 110 (2010) 6446–6473, <https://doi.org/10.1021/cr1002326>.
- [14] Z. Li, W. Luo, M. Zhang, J. Feng, Z. Zou, Photoelectrochemical cells for solar hydrogen production: current state of promising photoelectrodes, methods to improve their properties, and outlook, *Energy Environ. Sci.* 6 (2013) 347–370, <https://doi.org/10.1039/C2EE22618A>.
- [15] S.S. Kalanur, L.T. Duy, H. Seo, Recent progress in photoelectrochemical water splitting activity of WO₃ photoanodes, *Top. Catal.* 1–34 (2018), <https://doi.org/10.1007/s11244-018-0950-1>.
- [16] M. Harb, L. Cavallo, Toward the design of new suitable materials for solar water splitting using density functional theory, *ACS Omega* 3 (2018) 18117–18123, <https://doi.org/10.1021/acsomega.8b02884>.
- [17] C. Jiang, S.J.A. Moniz, A. Wang, T. Zhang, J. Tang, Photoelectrochemical devices for solar water splitting – materials and challenges, *Chem. Soc. Rev.* 46 (2017) 4645–4660, <https://doi.org/10.1039/C6CS00306K>.
- [18] A. Paracchino, V. Laporte, K. Sivula, M. Grätzel, E. Thimsen, Highly active oxide photocathode for photoelectrochemical water reduction, *Nat. Mater.* 10 (2011) 456–461, <https://doi.org/10.1038/nmat3017>.
- [19] I.V. Bagal, N.R. Chodankar, M.A. Hassan, A. Waseem, M.A. Johar, D.-H. Kim, S.-W. Ryu, Cu₂O as an emerging photocathode for solar water splitting - a status review, *Int. J. Hydrog. Energy.* 44 (2019) 21351–21378, <https://doi.org/10.1016/j.ijhydene.2019.06.184>.
- [20] L. Pan, Y. Liu, L. Yao, Dan Ren, K. Sivula, M. Grätzel, A. Hagfeldt, Cu₂O photocathodes with band-tail states assisted hole transport for standalone solar water splitting, *Nat. Commun.* 11 (2020) 318, <https://doi.org/10.1038/s41467-019-13987-5>.
- [21] H. Qi, J. Wolfe, D. Fichou, Z. Chen, Cu₂O photocathode for low bias photoelectrochemical water splitting enabled by NiFe-layered double hydroxide Co-catalyst, *Sci. Rep.* 6 (2016), 30882, <https://doi.org/10.1038/srep30882>.
- [22] D. Chen, Z. Liu, Z. Guo, W. Yan, Y. Xin, Enhancing light harvesting and charge separation of Cu₂O photocathodes with spatially separated noble-metal catalysts towards highly efficient water splitting, *J. Mater. Chem. A.* 6 (2018) 20393–20401, <https://doi.org/10.1039/C8TA07503D>.
- [23] C.-Y. Lin, Y.-H. Lai, D. Mersch, E. Reisner, Cu₂O|NiO_x nanocomposite as an inexpensive photocathode in photoelectrochemical water splitting, *Chem. Sci.* 3 (2012) 3482–3487, <https://doi.org/10.1039/C2SC20874A>.
- [24] K. Wetchakun, T. Samerjai, N. Tamaekong, C. Liewhiran, C. Siriwig, V. Kruefu, A. Visitsoraat, A. Tuantranont, S. Phanichphant, Semiconducting metal oxides as sensors for environmentally hazardous gases, *Sens. Actuators B Chem.* 160 (2011) 580–591, <https://doi.org/10.1016/j.snb.2011.08.032>.
- [25] P. Tyagi, A. Sharma, M. Tomar, V. Gupta, Efficient detection of SO₂ gas using SnO₂ based sensor loaded with metal oxide catalysts, *Procedia Eng.* 87 (2014) 1075–1078, <https://doi.org/10.1016/j.proeng.2014.11.349>.
- [26] P. Tyagi, A. Sharma, M. Tomar, V. Gupta, A comparative study of RGO-SnO₂ and MWCNT-SnO₂ nanocomposites based SO₂ gas sensors, *Sens. Actuators B Chem.* 248 (2017) 980–986, <https://doi.org/10.1016/j.snb.2017.02.147>.
- [27] N.L.W. Septiani, Y.V. Kaneti, B. Yuliarto, Nugraha, H.K. Dipojono, T. Takei, J. You, Y. Yamauchi, Hybrid nanoarchitecturing of hierarchical zinc oxide wool-ball-like nanostructures with multi-walled carbon nanotubes for achieving sensitive and selective detection of sulfur dioxide, *Sens. Actuators B Chem.* 261 (2018) 241–251, <https://doi.org/10.1016/j.snb.2018.01.088>.
- [28] I. Yoo, S.S. Kalanur, H. Seo, A nanoscale p–n junction photoelectrode consisting of an NiO_x layer on a TiO₂/Cds nanorod core-shell structure for highly efficient solar water splitting, *Appl. Catal. B Environ.* 250 (2019) 200–212, <https://doi.org/10.1016/j.apcatb.2019.02.063>.
- [29] I.-H. Yoo, Y.-J. Lee, S.S. Kalanur, H. Seo, Assembly of nonstoichiometric molybdenum oxide on Si as p–n junction photocathode for enhanced hydrogen evolution, *Appl. Catal. B Environ.* 264 (2020), 118542, <https://doi.org/10.1016/j.apcatb.2019.118542>.
- [30] Y. Xia, Z. He, J. Su, B. Tang, Y. Liu, Enhanced photocatalytic performance of Z-scheme Cu₂O/Bi₂O₃ nanocomposites, *J. Mater. Sci. Mater. Electron.* 29 (2018) 15271–15281, <https://doi.org/10.1007/s10854-018-9669-9>.
- [31] C. Cheng, C. Zhang, X. Gao, Z. Zhuang, C. Du, W. Chen, 3D network and 2D paper of reduced graphene oxide/Cu₂O composite for electrochemical sensing of hydrogen peroxide, *Anal. Chem.* 90 (2018), <https://doi.org/10.1021/acs.analchem.7b04070>, 1983–1991.
- [32] A. Naskar, S. Lee, K. Kim, Easy one-pot low-temperature synthesized Ag-ZnO nanoparticles and their activity against clinical isolates of methicillin-resistant *Staphylococcus aureus*, *Front. Bioeng. Biotechnol.* 8 (2020) 216, <https://doi.org/10.3389/fbioe.2020.000216>.
- [33] N. Kumar, K. Biswas, Cryomilling: an environment friendly approach of preparation large quantity ultra refined pure aluminium nanoparticles, *J. Mater. Res. Technol.* 8 (2019) 63–74, <https://doi.org/10.1016/j.jmrt.2017.05.017>.
- [34] A. Barrera, F. Tzompantzi, J. Campa-Molina, J.E. Casillas, R. Pérez-Hernández, S. Ulloa-Godínez, C. Velásquez, J. Arenas-Alatorre, Photocatalytic activity of Ag/Al₂O₃–Gd₂O₃ photocatalysts prepared by the sol–gel method in the degradation of 4-chlorophenol, *RSC Adv.* 8 (2018) 3108–3119, <https://doi.org/10.1039/C7RA12665D>.
- [35] D. Xue, J. Luo, Z. Li, Y. Yin, J. Shen, Enhanced photoelectrochemical properties from Mo-doped TiO₂ nanotube Arrays film, *Coatings* 10 (2020) 75, <https://doi.org/10.3390/coatings10010075>.
- [36] W. Zhong, S. Deng, K. Wang, G. Li, G. Li, R. Chen, H.-S. Kwok, Feasible route for a large area few-layer MoS₂ with magnetron sputtering, *Nanomaterials* 8 (2018) 590, <https://doi.org/10.3390/nano8080590>.
- [37] H. Wu, K. Lian, The development of pseudocapacitive molybdenum oxynitride electrodes for supercapacitors, *ECS Trans.* 58 (2014) 67, <https://doi.org/10.1149/05825.0067ecst>.